JOURNAL OF GEOPHYSICAL RESEARCH, VOL. 111, B10203, doi:10.1029/2005JB003854, 2006

Acoustic emission and velocities associated with the formation of compaction bands in sandstone

Jérôme Fortin,[1] Sergei Stanchits,[2] Georg Dresen,[2] and Yves Guéguen[1]

Received 31 May 2005; revised 2 May 2006; accepted 22 June 2006; published 7 October 2006.

[1] A series of laboratory experiments has been conducted in which three-dimensional (3-D) locations of acoustic emissions (AE) were recorded and used to analyze the development of compaction bands in Bleurswiller sandstone, which has a porosity of 25%. Results were obtained for saturated samples deformed under triaxial compression at three different confining pressures (60, 80, and 100 MPa), a pore pressure of 10 MPa, and room temperature. We recorded acoustic emissions, compressional and shear wave velocities, and porosity reduction under hydrostatic condition and under triaxial loading conditions at a constant axial strain rate. Our results show that seismic velocities and their amplitude increased during hydrostatic pressure build up and during initial axial loading. During shear-enhanced compaction, axial and radial velocities decreased progressively, indicating an increase of stress-induced damage in the rock. In experiments performed at confining pressures of 80 and 100 MPa during triaxial loading, acoustic emissions were localized in clusters. During progressive loading, AE clusters grow horizontally, perpendicular to the maximum principal stress direction, indicating formation of compaction bands throughout the specimens. Microstructural analysis of deformed specimens confirmed a spatial correspondence of AE clusters and compaction bands. For the experiment performed at a confining pressure of 60 MPa, AE locations and microstructural observations show symmetric compaction bands inclined to the cylinder axis of the specimen, in agreement with predictions from recent theoretical models.

Citation: Fortin, J., S. Stanchits, G. Dresen, and Y. Guéguen (2006), Acoustic emission and velocities associated with the formation of compaction bands in sandstone, *J. Geophys. Res.*, *111*, B10203, doi:10.1029/2005JB003854.

1. Introduction

[2] Brittle deformation of rocks frequently involves formation of narrow, localized bands on the grain scale that may evolve into macroscopic fracture zones. The micromechanics of fracture nucleation and growth in rocks have been investigated in a wealth of studies since the 1960s. The location of acoustic emission (AE) sources during deformation of rock has proven to be a useful nondestructive analytic technique to study the formation and growth of faults [*Lockner*, 1993; *Lei et al.*, 1992, 2000].

[3] Although dilatancy is generally observed as a precursor to brittle faulting and to the development of shear localization, recent field [*Mollema and Antonellini*, 1996] and laboratory [*DiGiovanni et al.*, 2000; *Olsson*, 1999; *Haimson*, 2001; *Klein et al.*, 2001; *Fortin et al.*, 2005] observations have also focused attention on the formation of localized compaction bands in porous sandstones. Laboratory experiments have shown that compaction bands occurred in dry and saturated sandstones with porosities ranging from 20 to 28%, deformed at room temperature. Formation of compaction bands was found to occur in homogeneous sandstones like Bentheim sandstone [*Klein et al.*, 2001], but also in sandstones containing clay or feldspars, such as Diemelstadt [*Fortin et al.*, 2003; *Baud et al.*, 2004], Castlegate [*Olsson*, 1999], and Bleurswiller sandstones [*Fortin et al.*, 2005].

[4] Compaction bands are narrow planar zones of material that formed without apparent shear. They extend in planes perpendicular to the main compressive stress. Compaction bands display significantly reduced porosity and act as barriers for fluid flow [*Holcomb and Olsson*, 2003; *Vajdova et al.*, 2004]. This suggests that the presence of compaction bands may affect fluid circulation in the crust, extraction of oil and gas from reservoir rocks, groundwater circulation in aquifers, as well as the sequestration of carbon dioxide.

[5] Reassessment of bifurcation theory produced theoretical models predicting the conditions required to localize deformation [*Rudnicki and Rice*, 1975; *Bésuelle and Rudnicki*, 2004; *Issen and Rudnicki*, 2000; *Rudnicki*, 2004]. These authors used a constitutive model with two-yield surfaces in the stress space; the shear yield surface provides a condition for the onset of dilatant, frictional failure while the onset of plastic compaction is represented by a yield cap. *Rudnicki* [2004] has analyzed conditions for both compaction band and shear band formation for stress states on an elliptic yield cap as applied to standard axisymmetric compression tests. His analysis also provides a

[1] Laboratoire de Géologie, Ecole Normale Supérieure, Paris, France.
[2] GeoForschungsZentrum, Potsdam, Germany.

0148-0227/06/2005JB003854$09.00

theoretical explanation for the occurrence of compacting shear bands at a very high angle to the compressive stress direction σ_1.

[6] In porous rock, micromechanisms involved in localized compaction are significantly different from those producing localized shear bands in dense rocks. In particular, grain crushing and pore collapse are associated with radiation of acoustic emissions [*Paterson*, 1978; *Zhang et al.*, 1990; *Olsson and Holcomb*, 2000]. More recently *DiGiovanni et al.* [2000] performed triaxial compression experiments on Castelgate sandstone and used electron and optical microscope investigations to elucidate the micromechanics of compaction. The authors found that acoustic emissions are associated with grain crushing and pore collapse.

[7] Effective elastic moduli of rocks and the velocity of elastic waves are significantly reduced in the presence of cracks [*Walsh*, 1965]. In deformation experiments at elevated pressures, elastic wave velocities are affected by two competing mechanisms [*Scott et al.*, 1993; *Fortin et al.*, 2005; *Schubnel et al.*, 2005]. With increasing mean pressure, velocities first increase due to elastic compaction and crack closure. When differential stress is increased further, localized grain crushing and the opening of new cracks will decrease the velocity of elastic waves. In this study, we investigate the nucleation and the growth of compaction bands in sandstone using advanced acoustic emission techniques. In particular, we investigate AE hypocenter locations and the evolution and anisotropy of compression and shear wave velocities.

[8] To address these issues, we performed triaxial compression experiments on Bleurswiller sandstone. *Fortin et al.* [2005] have shown that discrete compaction bands appeared in Bleurswiller sandstone in triaxial compression tests at effective confining pressures higher than 30 MPa (Figure 1). Here we report results from three triaxial compression experiments performed on saturated samples at a constant pore pressure of 10 MPa and confining pressures of 60, 80, and 100 MPa. In addition, a comparison between the acoustic emission locations and microstructural observations of a sample is made in order to relate the acoustic emission signature to the deformation microstructures.

2. Experimental Details

2.1. Rock Samples

[9] Specimens were prepared from Bleurswiller sandstone exposed in the Vosges mountains in eastern France (Frain Quarry). Bleurswiller is a gray sandstone containing 50% quartz, 30% feldspars, and 20% oxide micas. Porosity is about 25%. Grains are mostly subangular to subrounded. Grain size was determined from thin sections in the optical microscope using the linear intercept method and a correction factor of $\frac{3}{2}$, which accounts for the statistical unlikelihood of intercepting a grain across its full diameter [*Underwood*, 1970]. Grain sizes range from 80 to 150 μm with a mean value of approximately 110 μm. Cylindrical cores were cut from the same blocks of rock used in the *Fortin et al.* [2005] study and precision ground to yield specimens 50 mm in diameter and 100 mm in length.

2.2. Mechanical Data

[10] The experiments were performed at the GeoForschungsZentrum (Potsdam, Germany). We used a servocontrolled 4.6 MN loading frame from Material Test Systems (MTS) with a stiffness in compression of 11×10^9 N m^{-1}. All experiments were carried out at a constant axial strain rate of 10^{-5} s^{-1} at room temperature. The confining pressure was measured with an accuracy of 0.1 MPa, and during triaxial loading was held constant to within 0.5 MPa. Axial load was measured with an external load cell with an accuracy of 1 kN. Oil was used as the confining medium.

[11] Samples were saturated with distilled water and deformed under drained conditions at a constant pore pressure of 10 MPa. The variation of pore volume throughout a test was determined using a volumometer, allowing the evolution of connected sample porosity to be monitored.

[12] Axial strain, ε_z, was measured by a linear variable displacement transducer (LVDT) mounted at the end of the piston and corrected for the effective stiffness of the loading frame. Local axial strain, ε_z^*, and local radial strain, ε_r^*, measurements were acquired using strain gauges (TML FLA-20, Tokyosokki), each of which was glued directly to sample and mounted in a Wheatstone bridge. Uncertainty in strain was estimated to be 5×10^{-4} when calculated from the LVDT signal, and 10^{-5} when measured directly by the strain gauges. The local axial strain determined from the strain gauge measurements was different from the overall axial strain determined from the LVDT measurements, notably during the formation of compaction bands.

2.3. Acoustic Emissions

[13] Twelve piezoelectric transducers (PZT) each with a resonant frequency of 1 MHz were used in each triaxial test to determine the AE locations (Figure 2). The piezoceramic crystals were encapsulated in brass housings that conformed to the cylindrical surface of the sample. The housings were glued to the sample. Two additional P wave sensors were installed in the axial direction on the two end pieces (P_{11} and P_{12} in Figure 2). To monitor AE activity we used lead-zirconate-titanate piezoceramic discs 5 mm in diameter and 2 mm in thickness. After an amplification of 40 dB, fully digitized waveforms were recorded by a 10 MHz/16 bit data acquisition system (DaxBox, Prökel GmbH, Germany). Advanced software was used to automatically pick the onset time of AE signals and used for automated AE hypocenter determination. The hypocenter location algorithm is based on the downhill simplex algorithm [*Nelder and Mead*, 1965] modified for anisotropic and inhomogeneous velocity fields. AE hypocenter location error is estimated to be approximately 2.5 mm.

2.4. Elastic Wave Velocities

[14] The PZT transducers were also used for measuring P wave velocities during the experiments. The pulse transmission method was used to measure the elastic wave velocities. Receiver and source functions of the transducers were switched automatically. Monitoring deformation-induced changes in elastic wave velocities was necessary to accurately locate the AE hypocenters. In addition, elastic wave velocities are very sensitive to the presence of cracks, allowing one to detect whether compaction bands appeared with or without the formation of new cracks.

[15] In this experimental setup, P wave velocities were measured in directions perpendicular to the compressional axis, along five horizontal traces each passing through the

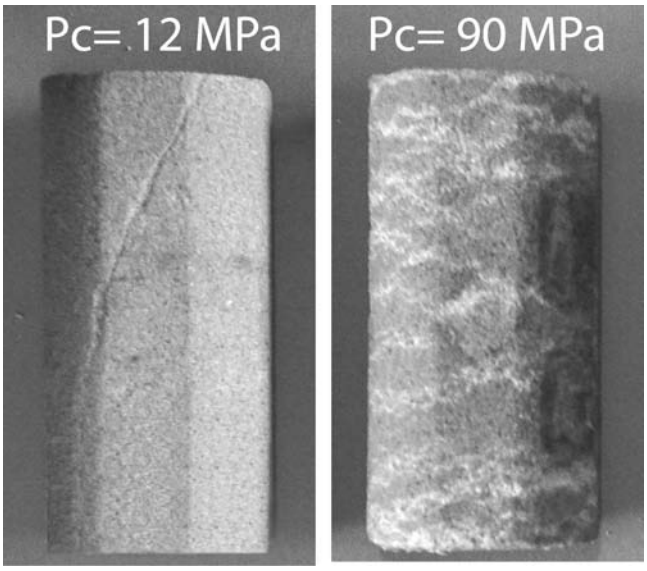

Figure 1. Bleurswiller sandstone (initial porosity is ~25%) fails by dilatant brittle faulting at effective pressures <30 MPa but develops shear-enhanced compaction at higher confining pressures. Compaction localization occurs over a wide pressure range (40–100 MPa). (a) Bleurswiller sandstone deformed at 2 MPa effective confining pressure showing a shear band. (b) Sample deformed at 80 MPa effective confining pressure (pore pressure was fixed at 10 MPa) showing discrete compaction bands (in white). The initial sample diameter was 40 mm, and the length was 80 mm.

center of the sample. Ultrasonic pulses were transmitted by transducers P_1, P_2, P_3, P_4, and P_5 and received (respectively) by transducers P_6, P_7, P_8, P_9, and P_{10} (Figure 2). Velocities were corrected for radial strain, ε_r, of the sample. During axial loading, the local radial strain value ε_r^* recorded by the strain gauges deviated from the LVDT-derived value due to localized compaction. For this reason, ε_r was calculated as follows: during hydrostatic loading $\varepsilon_r = \Delta\phi/3$, where $\Delta\phi$ is the change of porosity of the rock measured by the pore fluid volumometer. In axial loading $\varepsilon_r = (\Delta\phi - \varepsilon_z)/2$, where ε_z is the LVDT-derived axial strain. We assume that the volumetric strain of the sample equals the change of porosity of the sample. Finally, the radial P wave velocity $V_{P,\text{radial}}$ was calculated as the mean of the velocities measured along the five paths defined above. To monitor fracture-induced anisotropy, two additional P wave sensors were installed in axial direction (P_{11} and P_{12}) measuring P wave velocity $V_{P,\text{axial}}$ parallel to the compressional axis (Figure 2). Measurements were corrected for axial deformation, ε_z. We assumed that $\varepsilon_z = \varepsilon_r$ during hydrostatic loading. Four polarized S wave piezoelectric sensors were glued to the cylindrical surface of the samples (Figure 2) with one pair oriented in a horizontal direction for measuring S_h and one pair oriented in a vertical direction for measuring S_v. Shear wave PZTs were plates 10 × 10 × 1 mm in dimension. As for the radial P wave velocities, S wave velocities were corrected for radial strain, ε_r.

[16] The transmitted elastic waveform was digitized and logged by a computer every 40 s. To calculate velocities from the recorded traveltimes, we corrected for variations in traveltimes associated with transmission through the transducer brass housings and spacers. The error in absolute

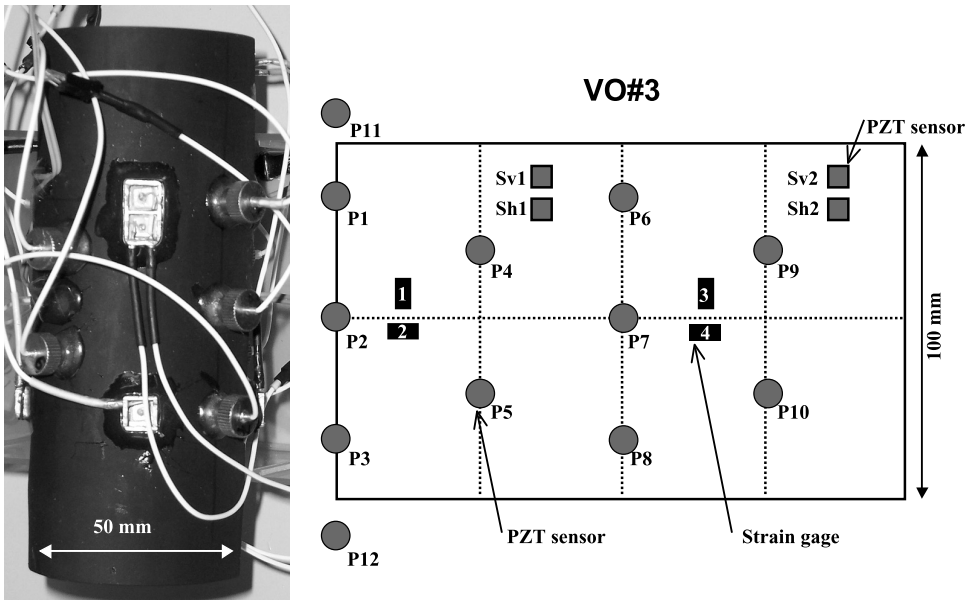

Figure 2. (a) Sample setup used in this study. The initial sample diameter and length were 50 and 100 mm, respectively. (b) Map of the outside surface of the sample showing locations of 12 PZT sensors plus 4 S wave sensors and four strain gauges. Sensors 11 and 12 were mounted on the two end pieces. The PZT sensors were used to monitor AE activity and P wave velocities during the experiments. Samples were jacketed in neoprene sleeves.

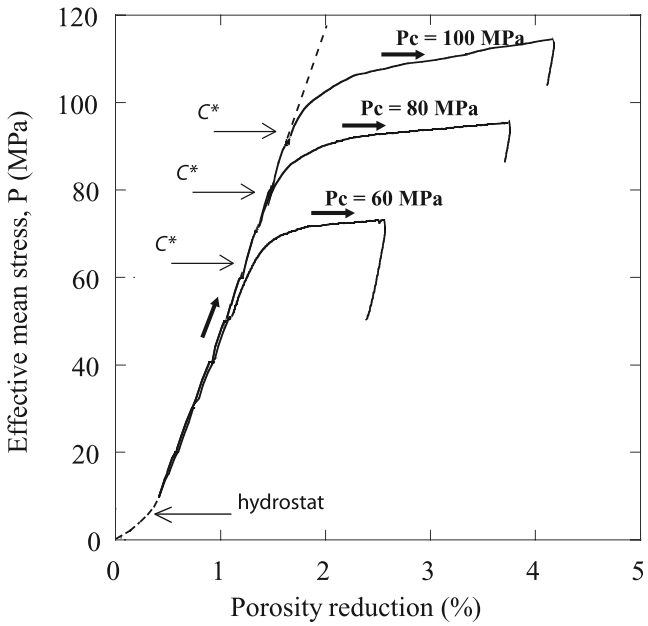

Figure 3. Effective mean stress versus porosity reduction for three triaxial experiments performed at P_c = 60 MPa, P_c = 80 MPa, and P_c = 100 MPa. For reference, hydrostatic loading is shown as a dashed line. The critical stress states C^* are indicated by arrows.

velocity is estimated to be less than 2% but the relative error between two consecutive measurements was reduced to 0.5% using an advanced technique for picking arrival times.

2.5. Experimental Procedure

[17] During each experiment, confining pressure was first increased to 5 MPa. Pore pressure and confining pressure were then increased simultaneously to 1 and 6 MPa, respectively. Pressure was held constant for at least 12 hours to obtain full fluid saturation of the samples. At the beginning of each experiment, the pore pressure and confining pressure were increased to 10 and 20 MPa, respectively. Three experiments were conducted at confining pressures of 60, 80, and 100 MPa. At the end of each experiment, the sample was carefully unloaded and recovered for microstructural analysis. Samples were wrapped in copper foils and enclosed in neoprene jackets to insulate them from the oil used as the confining medium. Experiments were typically stopped at axial strains of approximately 3%.

3. Results

3.1. Summary of Mechanical Data

[18] In this paper, we use the convention that compressive stresses and compactive strains are positive. The maximum and minimum (compressive) principal stresses are denoted by σ_1 and σ_3, respectively. The pore pressure is denoted by P_p, and the difference between the confining pressure ($P_c = \sigma_2 = \sigma_3$) and the pore pressure is referred to as "the effective pressure." The effective mean stress $(\sigma_1 + 2\sigma_3)/3 - P_p$ will be denoted by P and the differential stress $\sigma_1 - \sigma_3$ by Q.

[19] *Fortin et al.* [2005] have shown that for Bleurswiller sandstone no dilatancy is observed for effective confining pressures higher than 30 MPa. The results for the three experiments conducted at confining pressure of 60, 80, and 100 MPa are summarized in Figure 3. In all of our experiments, confining pressure was first increased to the final level before samples were loaded by axial compression. As long as a hydrostatic pressure was applied, sample compaction remained purely elastic following the hydrostatic loading (dashed) curve in Figure 3. With increasing differential stress, however, inelastic compaction started at a critical stress state C^*. At stress levels beyond C^*, the differential stress induced a significant compactive strain, referred to as shear-enhanced compaction [*Wong et al.*, 1997]. Mechanical data for the three experiments are given in Table 1.

3.2. Elastic Wave Velocities

[20] The effects of confining pressure and differential stress on the velocities $V_{P,\text{radial}}$, $V_{P,\text{axial}}$, V_{Sv}, and V_{Sh} were analyzed during the three experiments. Figure 4 summarizes the velocity measurements for sample Vo3 (in this experiment, confining pressure was 80 MPa). We plot the elastic wave velocities as a function of porosity (Figure 4c) and effective mean stress (Figure 4d). For reference, the porosity reduction versus effective mean stress is given in Figure 4a.

[21] During hydrostatic loading, P and S wave velocities first increase as shown in Figure 4. Figure 4d shows that the P wave, S_h wave, and S_v wave velocities reach a plateau at 3.57, 2.12, and 2.1 km s^{-1}, respectively. A velocity increase is also observed at the beginning of axial loading. However, we found a striking agreement between the onset of inelastic compaction at C^* and a decrease in elastic wave velocities. Figure 4b shows the amplitude variation for the radial P wave velocities. The amplitude is normalized by the initial amplitude measured at the beginning of the experiment. The amplitude exhibits a large increase upon initial loading by almost 40%, followed by a rapid decrease during shear-enhanced compaction to about 60% of its maximum value. The observed anisotropy of the velocity field may be expressed by two parameters [*Thomsen*, 1986]:

$$\Sigma = \frac{V_{P,\text{radial}}^2 - V_{P,\text{axial}}^2}{2\,V_{P,\text{axial}}^2} \qquad \text{and} \qquad \gamma = \frac{V_{Sh}^2 - V_{Sv}^2}{2\,V_{Sv}^2}\ .$$

[22] Figures 4e and 4f show the evolution of velocity anisotropy parameters Σ and γ as functions of porosity reduction and effective mean stress, respectively. Note that the initial anisotropy of the rock is less than 5% for the shear velocity and lower than 2% for the compressional velocity.

Table 1. Compilation of Mechanical Data for Bleurswiller Sandstone Samples for the Three Experiments

	Confining Pressure P_c, MPa	Effective Mean Stress P at C^*, MPa	Differential Stress Q at C^*, MPa	Maximum Axial Strain, %	Comments on Failure Modes
Vo2	60	67	51	2.3	discrete "compacting shear" bands
Vo3	80	85	45	3.2	discrete compaction bands
Vo1	100	99	27	2.2	discrete compaction bands

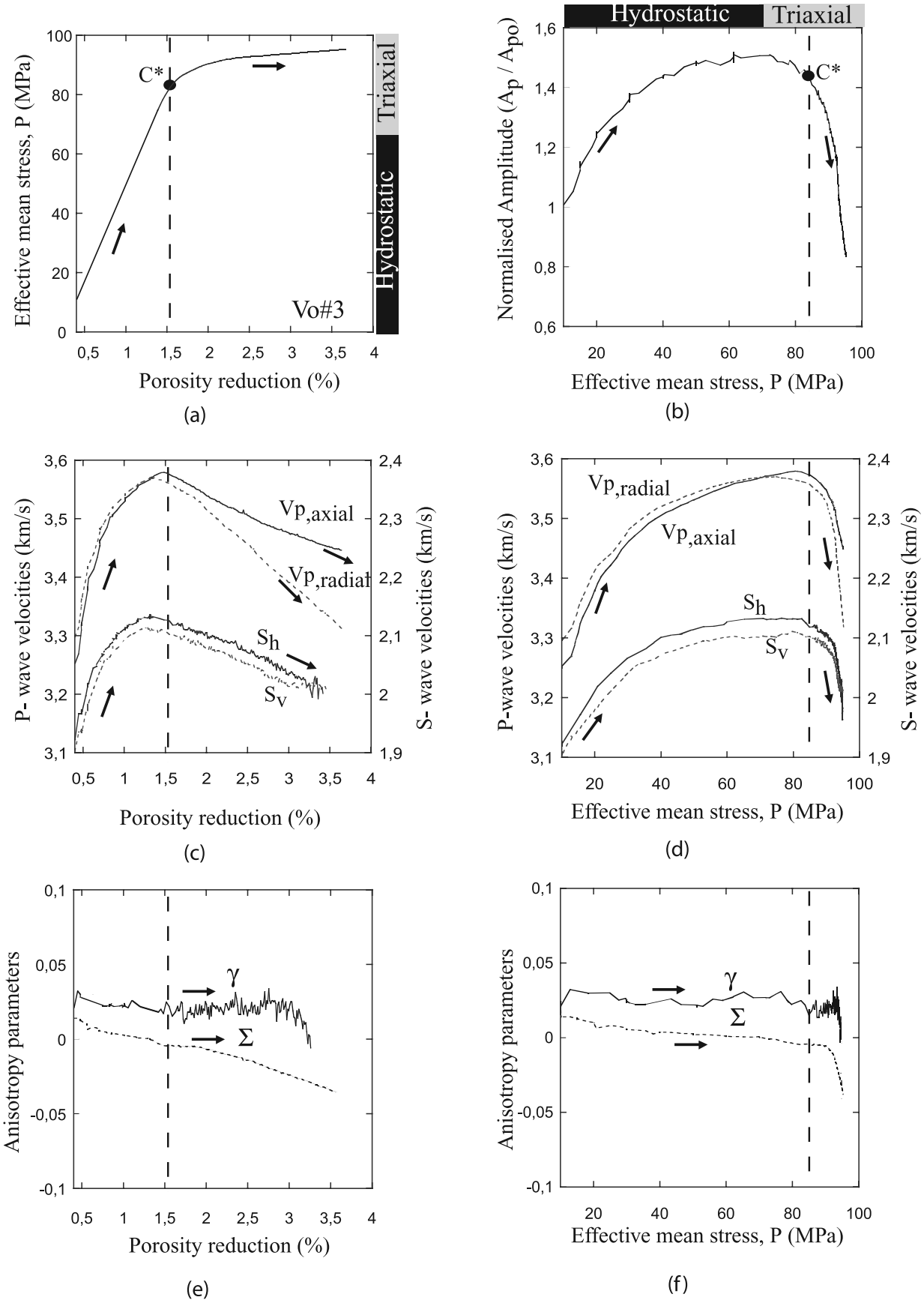
Effective mean stress, P (MPa)
C*
Vo#3
Triaxial
Hydrostatic
Porosity reduction (%)
(a)
Normalised Amplitude (Ap / Apo)
Hydrostatic
Triaxial
C*
Effective mean stress, P (MPa)
(b)
P- wave velocities (km/s)
S- wave velocities (km/s)
Vp,axial
Vp,radial
Sh
Sv
Porosity reduction (%)
(c)
P-wave velocities (km/s)
S- wave velocities (km/s)
Vp,radial
Vp,axial
Sh
Sv
Effective mean stress, P (MPa)
(d)
Anisotropy parameters
γ
Σ
Porosity reduction (%)
(e)
Anisotropy parameters
γ
Σ
Effective mean stress, P (MPa)
(f)

Figure 4

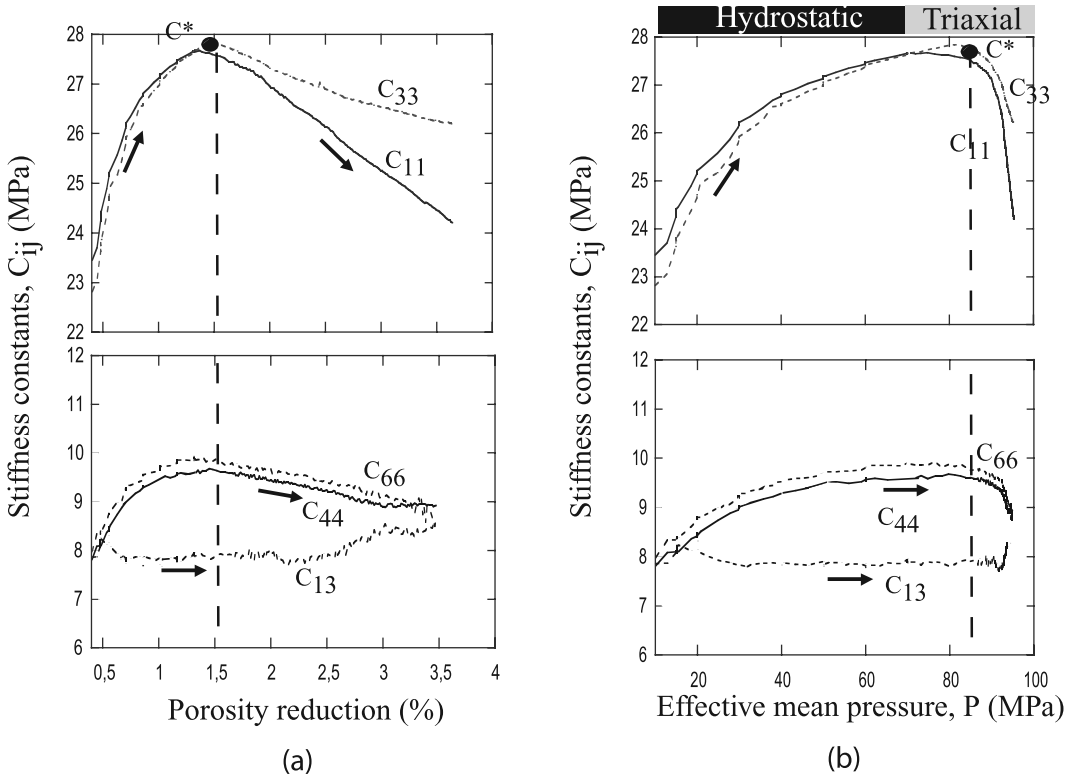

Figure 5. Elastic moduli estimated from ultrasonic velocity measurements using a transverse isotropic velocity model corrected for bulk density ρ changing during the experiment. Elastic moduli C_{ij} are shown as a function of (a) porosity reduction and (b) effective mean stress. Note that the evolution of the elastic moduli C_{ij} follows the same pattern as that observed for the elastic wave velocities (Figure 4). At C^* the elastic constants decrease, likely due to the nucleation of new cracks at high confining pressure.

During hydrostatic loading and the first part of the triaxial loading, the anisotropy remains low: Σ decreases from 2% to 0%, and γ fluctuates around a constant value. When the stress state reaches at C* the beginning of shear-enhanced compaction, the compressional anisotropy as measured by Σ decreases from 0% to -3%. The anisotropy of shear wave velocity as measured by γ remains constant during the entire experiment. The behavior of the anisotropy parameters during the experiments indicates that the formation of compaction bands does not produce a strong elastic anisotropy.

3.3. Elastic Moduli

[23] In isotropic rock, elastic wave velocities are expressed as

$$V_p = \sqrt{\frac{K + \frac{4}{3}\mu}{\rho}} \quad \text{and} \quad V_s = \sqrt{\frac{\mu}{\rho}},$$

where K is the bulk modulus, μ the shear modulus, and ρ the bulk density of the rock. A decrease of P and S wave velocities during shear-enhanced compaction may indicate the formation of cracks affecting the bulk modulus K and the shear modulus μ. Because of compaction, the bulk sample porosity decreases and the bulk density increases. However, the formation of new cracks contributes very little to changes in sample porosity, which is dominated by a porosity decrease resulting from shear-enhanced compaction. The combined effect of density increase and reduction of elastic moduli results in a net decrease of elastic wave velocities.

[24] To eliminate the bulk density effect, we invert the elastic moduli from the velocity measurements using a transverse isotropic velocity model. This model accounts for the observed small elastic anisotropy due to the presence of the compaction bands. We define a Cartesian coordinate system with x and y axes perpendicular, and the z axis parallel to the sample cylinder axis. In the transverse isotropic model, elastic properties are isotropic in directions

Figure 4. Mechanical data and velocity measurements for the triaxial compression experiment Vo3 performed at 80 MPa confining pressure. (a) Effective mean stress versus porosity reduction, (b) amplitude of the radial velocities as a function of effective mean stress, (c) P and S wave velocities plotted versus porosity reduction and (d) versus effective mean stress, and (e) and (f) elastic anisotropy parameters [*Thomsen*, 1986] versus porosity reduction and effective mean stress, respectively. The critical stress state C^* at the onset of shear-enhanced compaction is indicated by a dashed line. Note that velocities and their amplitudes decrease at C^*. Anisotropy parameters Σ and γ indicate that the formation of compaction bands does not result in a strong anisotropy of elastic wave velocities.

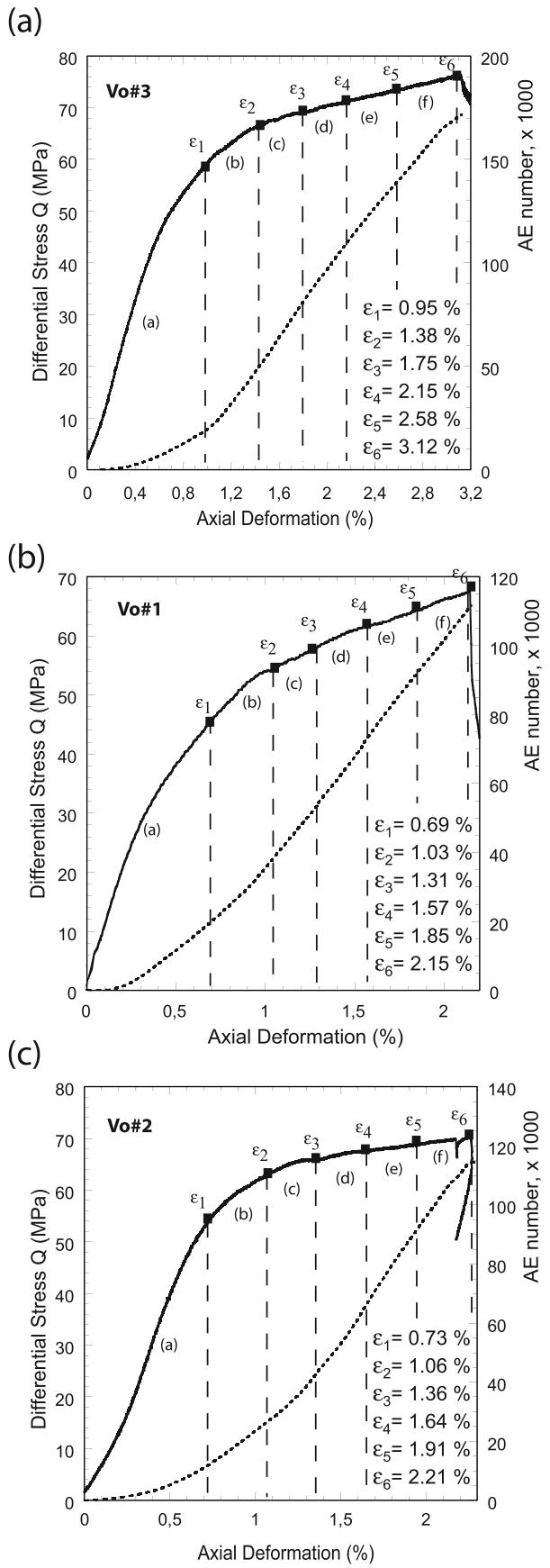

perpendicular to z but change along the z axis. The elastic stiffness tensor C_{ij} has five independent constants, C_{11}, C_{33}, C_{44}, C_{66}, and C_{13}:

$$\begin{pmatrix} C_{11} & C_{12} & C_{13} & 0 & 0 & 0 \\ C_{12} & C_{11} & C_{13} & 0 & 0 & 0 \\ C_{13} & C_{13} & C_{33} & 0 & 0 & 0 \\ 0 & 0 & 0 & C_{44} & 0 & 0 \\ 0 & 0 & 0 & 0 & C_{44} & 0 \\ 0 & 0 & 0 & 0 & 0 & C_{66} \end{pmatrix}$$

where

$$C_{12} = C_{11} - 2\,C_{66}.$$

[25] These five independent C_{ij} constants are related to the five elastic wave velocities measured experimentally as follows [*Mavko et al.*, 1998]:

Quasi-longitudinal mode

$$V_P(\theta) = \left(C_{11}\sin^2\theta + C_{33}\cos^2\theta + C_{44} + \sqrt{M}\right)^{1/2}(2\rho)^{-1/2}$$

Quasi-shear mode

$$V_{Sv}(\theta) = \left(C_{11}\sin^2\theta + C_{33}\cos^2\theta + C_{44} - \sqrt{M}\right)^{1/2}(2\rho)^{-1/2}$$

Pure shear mode

$$V_{Sh}(\theta) = \left(\frac{C_{66}\sin^2\theta + C_{44}\cos^2\theta}{\rho}\right)^{1/2}$$

where

$$M = \left[(C_{11} - C_{44})\sin^2\theta - (C_{33} - C_{44})\cos^2\theta\right]^2 + (C_{13} + C_{44})^2\sin^2 2\theta$$

and θ is the angle between the wave vector and the axis of symmetry, which here is the vertical z axis. The five components of the stiffness tensor were obtained from the measurement of five velocities: $V_P(0°)$ ($=V_{P,\mathrm{axial}}$), $V_P(90°)$ ($=V_{P,\mathrm{radial}}$), $V_P(40°)$, $V_{Sh}(90°)$, and $V_{Sv}(90°)$. Figures 5a and 5b illustrate the evolution of the dynamic stiffness parameters C_{ij} as functions of porosity reduction and effective mean stress, respectively. The evolution of the dynamic stiffnesses is closely related to the observed changes in the elastic wave velocities, illustrating the complex relation between porosity and elastic properties.

Figure 6. Differential stress (solid curve) and cumulative acoustic emissions (dotted curve) as a function of axial strain in Bleurswiller sandstone. (a) P_c = 80 MPa (experiment Vo3). (b) P_c = 100 MPa (experiment Vo1). (c) P_c = 60 MPa (experiment Vo2). Six stress-strain increments are defined for each experiment (a–f) corresponding to the AE hypocenter distributions shown in Figures 7, 8, and 9.

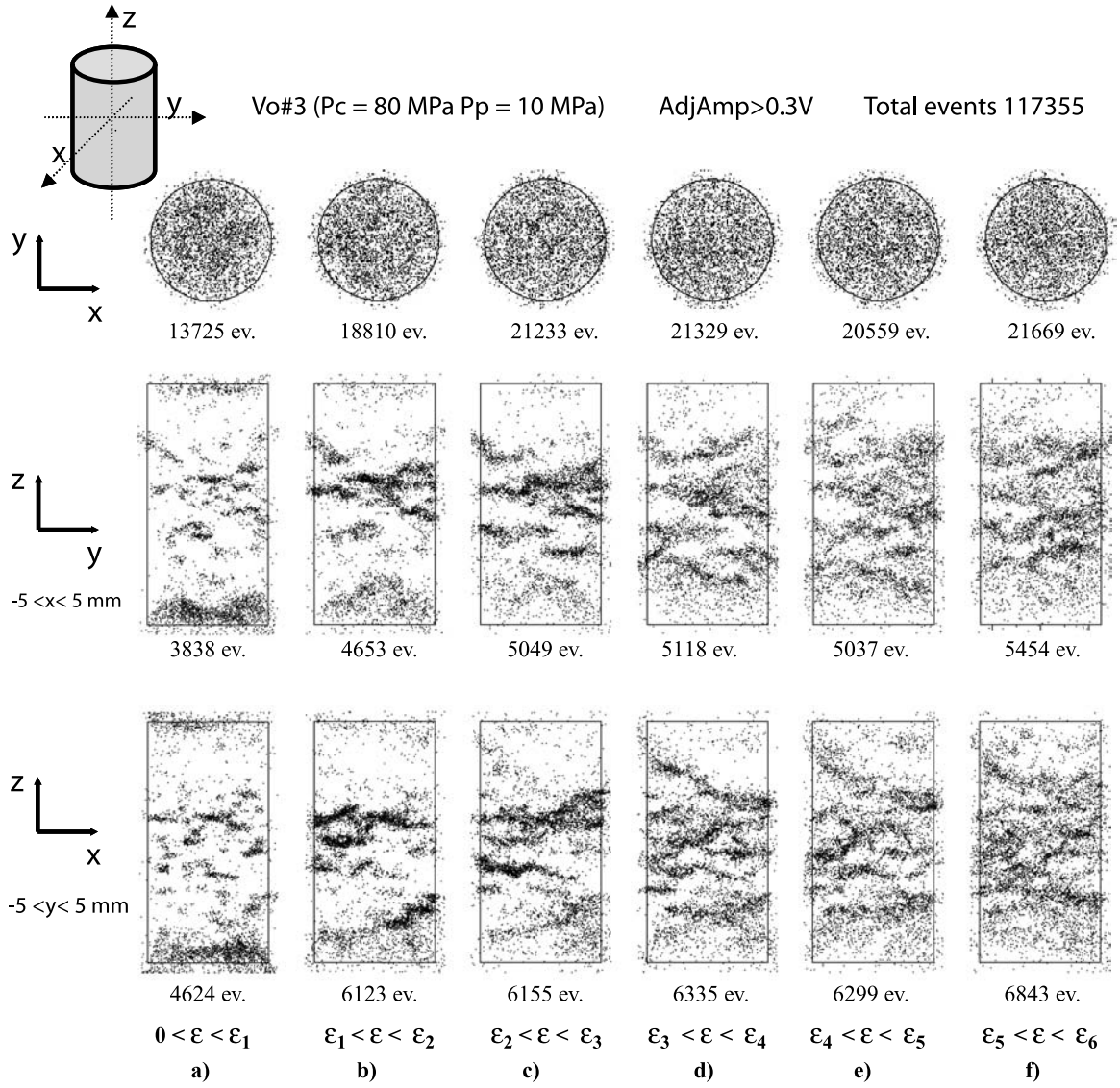

Figure 7. AE hypocenter distribution for sample Vo3. The strain increments are defined in Figure 6a. Confining pressure and pore pressure were 80 and 10 MPa, respectively. (top) A view looking down on sample (projection of all events on to the (y, x) plane). (middle) A projection of all the events located between -5 mm $< x <$ $+5$ mm on the (z, y) plane. (bottom) Face-on view in which sample has been rotated counterclockwise 90° (projection of all the events located between -5 mm $< y <$ $+5$ mm on the (z, x) plane). Each point represents one AE event. AE events form clusters that are elongated mostly perpendicular to the compression direction (z axis). The maximum axial strain is 3.12%.

3.4. Acoustic Emissions

[26] Brittle faulting has been thoroughly studied in the laboratory. Different authors have used acoustic emission techniques in triaxial tests performed on low-porosity rocks and sandstones to investigate shear fracture nucleation [*Lockner*, 1993; *Lei et al.*, 1992, 2000; *Zang et al.*, 1998, 2000]. Adopting strain rate or acoustic emission rate as feedback to servocontrol axial loading, previous authors used AE hypocenter locations to map microcrack clustering and localization. The data provides important constraints for a theoretical analysis of the onset of shear localization.

[27] We determined AE hypocenter locations in three triaxial compression experiments performed on Bleurswiller sandstone. In our experiments formation of discrete compaction bands occurred throughout the entire sample volume. Located AE events form clusters that closely coincide in space with compaction bands observed in the optical microstructure of the deformed specimens (see section 4).

3.4.1. Acoustic Emission Hypocenters

[28] Constant strain rate deformation of sample Vo3 at 80 MPa confining pressure is characterized by strain hardening and shear-enhanced compaction (Figure 6a). We recorded more than 170,000 AE events of which more than 117,000 were located (Figure 7). Strain increments a–f in Figure 6a correspond to the AE hypocenter distributions a–f shown in Figure 7 in projections parallel to the x, y, and z axes. The location error was ±2 mm.

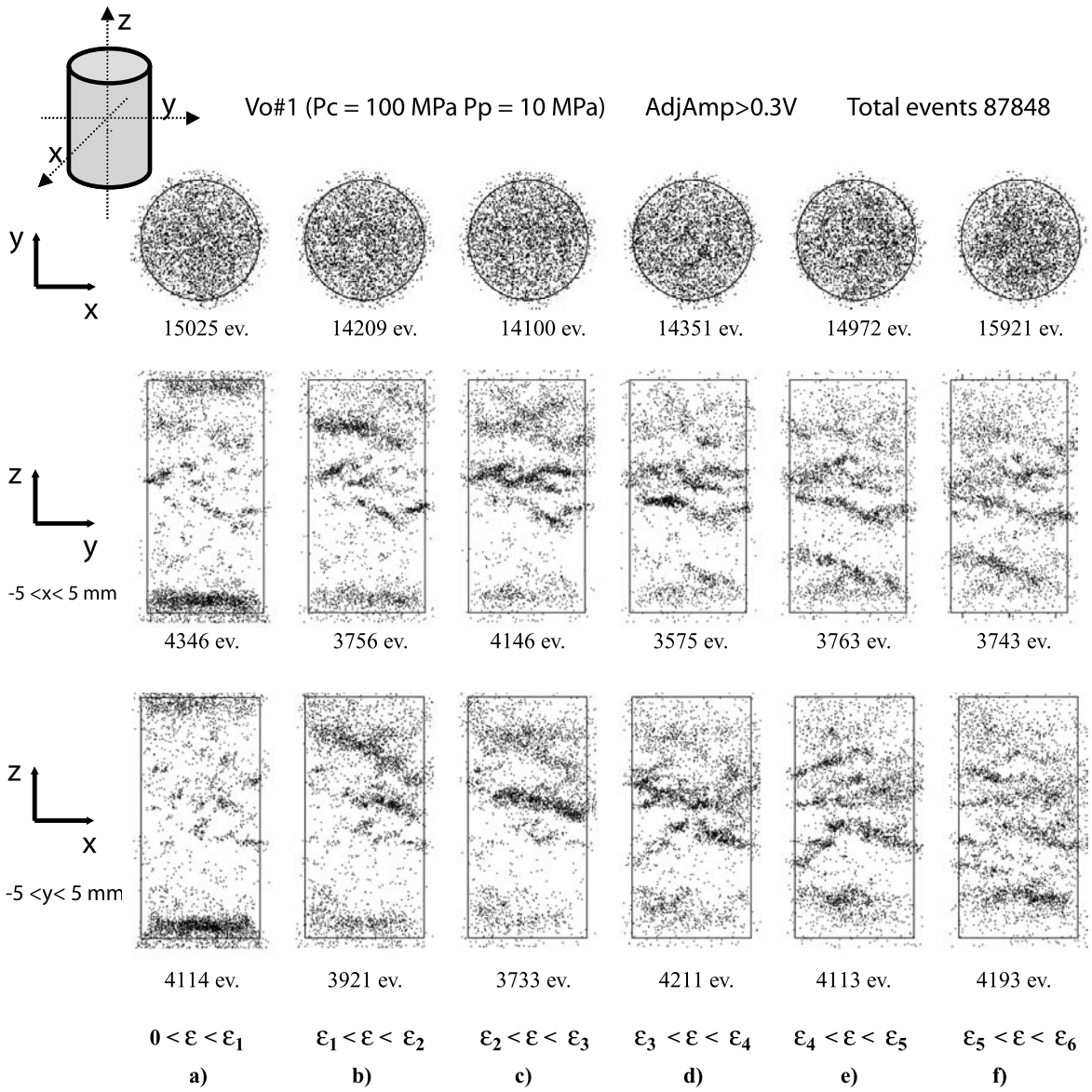

Figure 8. AE hypocenter distribution for sample Vo1 (see Figure 7). The different strain increments during the loading are defined in Figure 6b. Confining pressure and pore pressure were 100 and 10 MPa, respectively. Note that at a confining pressure of 100 MPa, clustering of AE events and formation of compaction bands are very similar to those occurring in the experiment performed at the lower confining pressure of 80 MPa. In this experiment, the maximum axial strain is 2.15%.

[29] AE clusters first form both in the sample interior and at the specimen ends. The latter may be related to inhomogeneous stresses owing to end cap friction. Pronounced localization of AE hypocenters occurs in stage b of Figure 7 indicating that sample deformation is characterized by shear-enhanced compaction (Figure 3). AE events form clusters that are elongated perpendicular to the compression direction.

[30] At a confining pressure of 80 MPa, Bleurswiller sandstone develops discrete compaction bands with a thickness of about 0.5–2 mm, which is roughly 5–20 times the average grain size. This is confirmed from postmortem microstructure observations (see section 4 and also *Fortin et al.* [2005]). The compaction bands are not perfectly planar and grow laterally by coalescence of pore collapse clusters (Figure 7). Once a compaction band cuts through the entire sample, the process repeats itself and new bands form above and below older ones. Finally, AE hypocenters indicate several discrete bands crosscutting the sample in agreement with the observations of deformation microstructures.

3.4.2. Influence of Confining Pressure

[31] Sample Vo1 was deformed at a confining pressure of 100 MPa. The different loading stages and the corresponding hypocenter distributions are shown in Figures 6b and 8. The total number of events for Vo1 is somewhat less than for Vo3 since the axial strain was only 2.15% for Vo1 compared to 3.12% for Vo3.

[32] The clustering of AE events and compaction band formation for Vo1 are very similar to that observed in the experiment performed at a lower confining pressure of 80

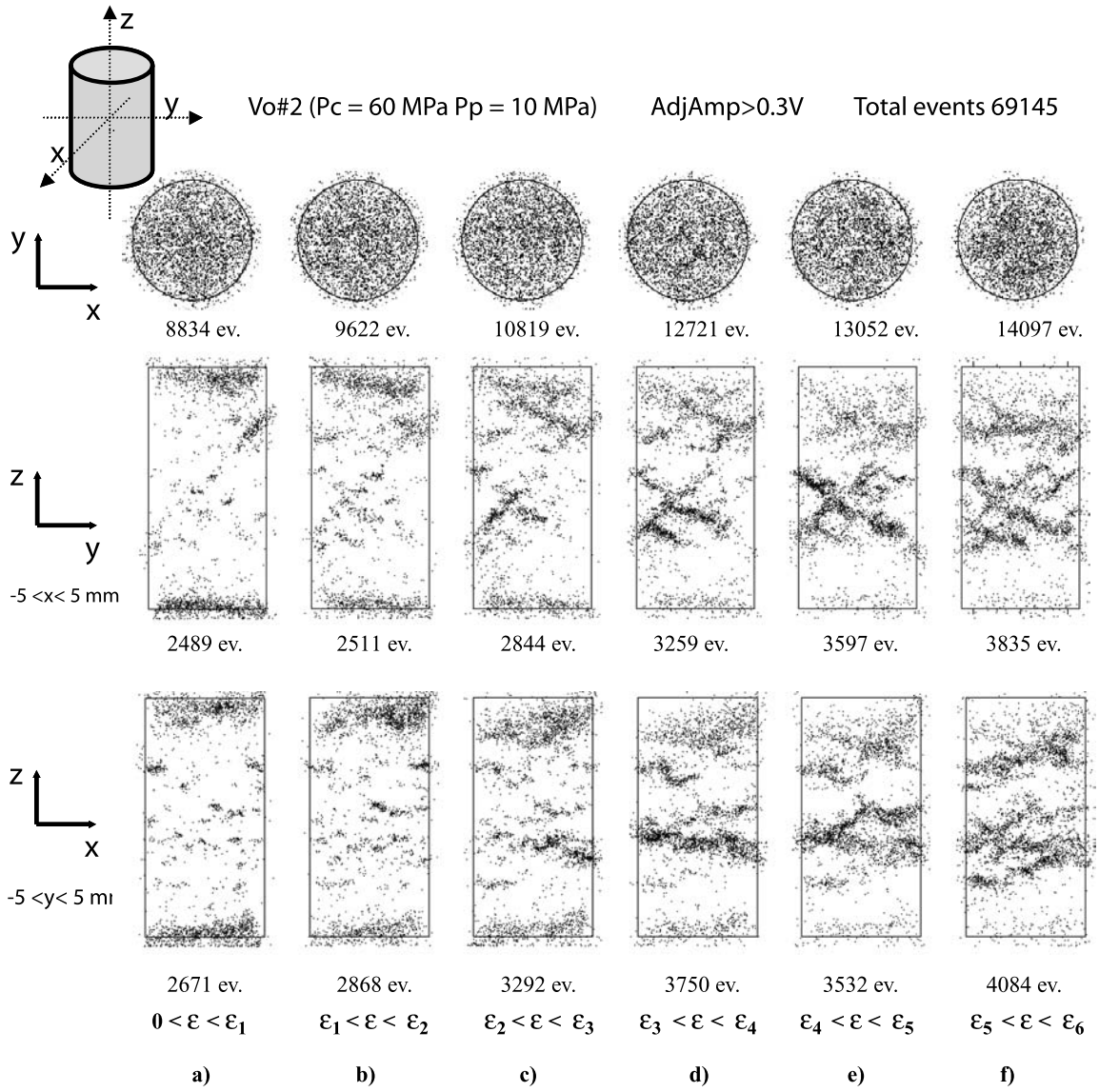

Figure 9. AE hypocenter distribution for sample Vo2 (see Figure 7). The different strain increments during the loading are defined in Figure 6c. Confining pressure and pore pressure were 60 and 10 MPa, respectively. The clustering of AE events in Figure 9 (bottom) is similar to that observed in Figures 7 and 8, but Figure 9 (middle) reveals discrete bands oriented to the compression stress direction (*z* axis) consistent with predictions from recent theoretical models. In this experiment, the maximum axial strain is 2.21%.

MPa (compare Figures 8 and 7). At an axial strain of 2.15%, the AE locations highlight five discrete compaction bands.

[33] We conducted a third experiment at a confining pressure of 60 MPa (Figures 6c and 9). More than 120,000 AE events were recorded, and more than 69,000 events were located. Orientations of AE clusters and bands were different from those observed in experiments performed at higher confining pressures (Figure 9). In particular, the y-z projection of the AE hypocenter distribution reveals discrete conjugate bands oriented at an angle of about 60° to the compressive stress direction σ_1.

4. Microstructural Observations

[34] We performed detailed microstructural studies on deformed samples using optical microscopy and scanning electron microscopy (SEM). To prepare SEM sections, samples 25 × 50 mm in size were cut parallel to the long specimen axis and the maximum compressive stress σ_1 direction (Figure 10). Pore water was removed by drying. Sections were impregnated with blue epoxy to aid in the identification of open pore space and subsequently polished and gold coated.

[35] Sections of the entire sample reveal numerous, narrow, compaction bands that are clearly visible to the naked eye. For example, three prominent bands formed in the interior of sample Vo2, as shown in Figure 10. An incipient band spanning halfway across the sample is revealed in the top part of the specimen. The three discrete compaction bands, zones α, β, and χ, in Figure 10a, coincide closely with the clustering of acoustic emission locations in Figure 10b. In general, the AE hypocenter distribution

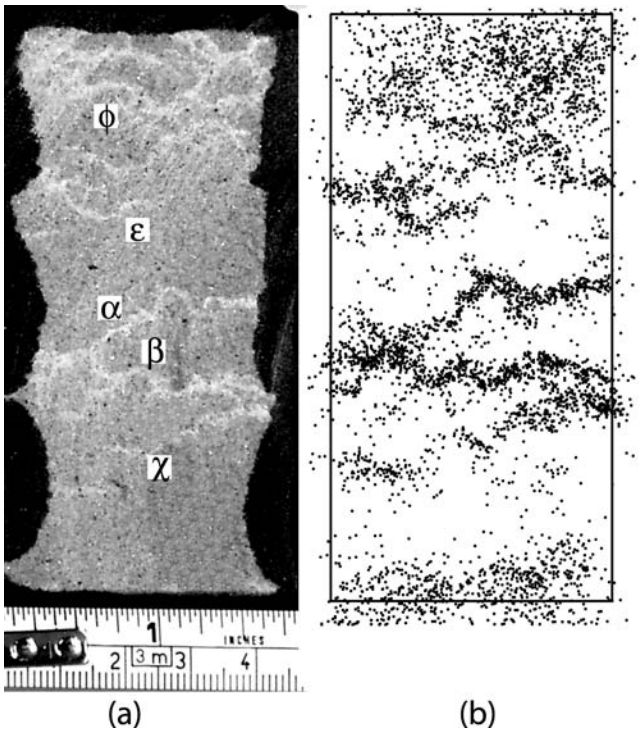

Figure 10. Comparison of (a) longitudinal section of deformed sample Vo2 and (b) associated AE hypocenter locations. In Figure 10a, dark color indicates epoxy, and Greek letters denote prominent compaction bands. In Figure 10b, locations of all events recorded during loading of sample Vo2 in (z, x) projection are shown. The AE hypocenter distribution shows excellent agreement with the location of deformation bands (see zones α, β,χ, and ε).

shows excellent agreement with the location of deformation bands (compare Figures 10a and 10b). AE events form several clusters but no bands formed near the specimen ends. In Figure 10b, we plotted 3200 acoustic emission events located in the volume of Figure 10a, i.e., in the (z, x) plane between $y = -1.5$ mm and $y = +1.5$ mm. Note that the shape of the compaction band (α) is mirrored exactly by the shape of the AE hypocenter clusters. Diffuse AE clusters formed at the specimen top and bottom ends, likely due to end cap friction. With progressive loading AE activity close to the specimen ends becomes less pronounced. The close correspondence between microstructure and AE hypocenter distribution shows that the latter are an excellent proxy for studying the nucleation and growth of compaction bands.

[36] In SEM, a compaction band 0.6 mm in thickness appears as a crushed zone of reduced porosity (Figure 11, zone I). Outside the band, the microstructure of the rock remains largely undeformed (Figure 11, zone II) with a porosity of about 25%. Inside the band, the grains are completely crushed and the fragments fill up the collapsed pore space (Figure 12). Inside the band the porosity is less than 5% and cracks occur at grain-grain contacts (Figure 12b). The resulting fragments fill the existing pores leading to a decrease in porosity of the samples. Frequently, clay minerals are present in the pore lining and contribute with the cement to filling the pore space.

5. Discussion

5.1. Yield Surface

[37] Bleurswiller sandstone fails by dilatant brittle faulting at effective pressures less than 30 MPa (Figure 13). At effective pressures higher than 40 MPa, the yield surface shows a cap.

[38] At effective confining pressure higher than 40 MPa, shear-enhanced compaction starts when the compactive yield stress C^* is reached. Compaction localization occurs over a wide pressure range (40–100 MPa). This domain of compaction localization may be divided in to two subdomains. For effective confining pressures ranging from 40 to 50 MPa, we observed low-angle compaction bands oriented $\sim 60^\circ$ to σ_1, in agreement with previous experimental investigations [*Bésuelle*, 2001]. *Bésuelle* [2001] has modeled the evolution of volumetric strain inside the band, predicting a progressive and continuous change from dilating shear bands, to compacting shear bands, to pure

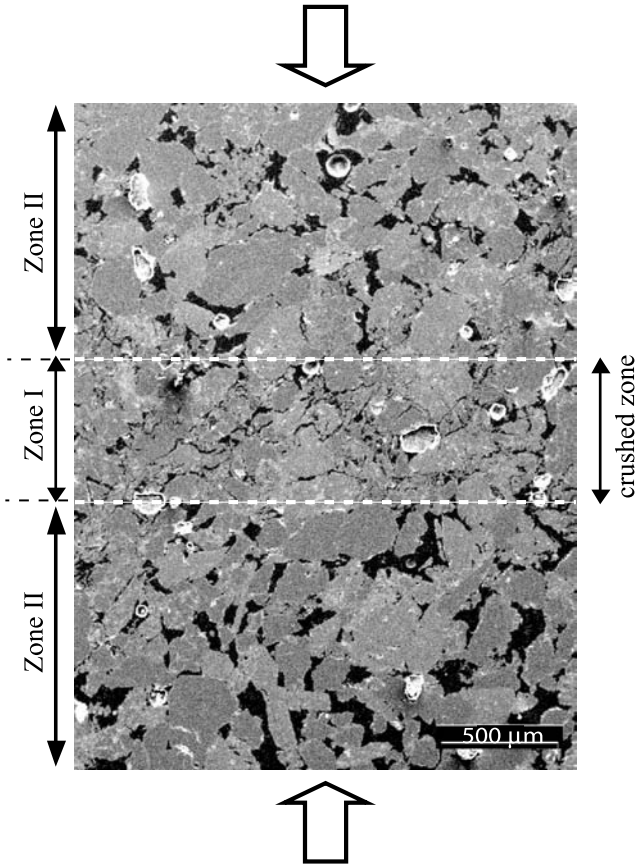

Figure 11. SEM micrograph (backscattered electron image) of Bleurswiller sandstone loaded in triaxial compression. Maximum compressive stress is vertical. Epoxy-filled pores appear in black. Zone I is a compaction band with a thickness of 0.6 mm. Inside the compaction band, the porosity is less than 5% due to grain crushing and pore collapse. In zone II, the porosity is close to the initial porosity of the rock (25%).

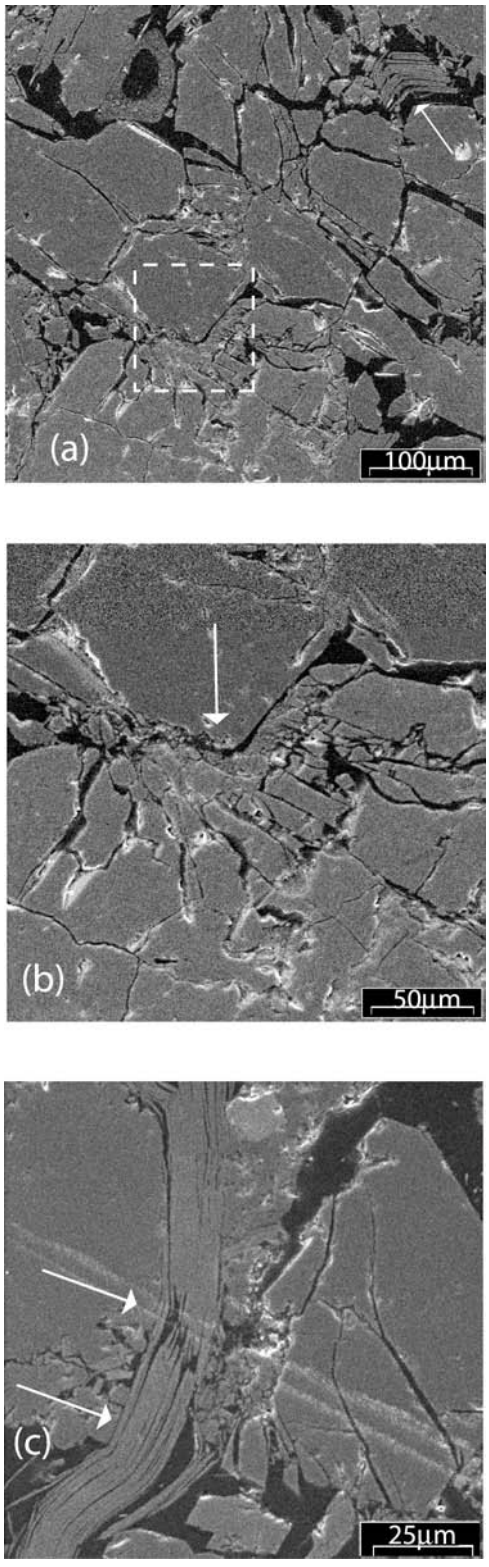

Figure 12. Backscattered SEM micrograph revealing details inside the compaction band. Maximum compressive stress direction is vertical. (a) Crushed quartz grains and cement fragments filling pore space (in black), (b) cracks at grain-grain contacts, and (c) deformed clay minerals indicating displacement of neighboring quartz grains.

compacting (no shear) bands with increasing confining pressure. More recently, *Rudnicki* [2004] used an elliptic yield cap model that predicts the occurrence of compaction bands within a range of confining pressures close to the transition between brittle and ductile material behavior. In our experiments, the formation of discrete compaction bands in subparallel arrays perpendicular to the compression direction occurs over a pressure range of 60–100 MPa.

[39] The shape of the yield envelope for Bleurswiller sandstone may be compared to theoretical models. *Wong et al.* [1997] have shown that yield envelopes for sandstone data can be described by an elliptical cap in P-Q stress space defined by the equation:

$$\frac{(P/P^* - \xi)^2}{(1-\xi)^2} + \frac{(Q/P^*)^2}{\varsigma^2} = 1 \ ,$$

where P^* is the mean stress at the beginning of grain crushing and pore collapse under hydrostatic pressure and ξ and ς are two constants. More recently *Grueschow* [2005] has generalized the yield envelope to a "*n* power model" and expressed the yield surface as

$$\left(\frac{P}{a}\right)^n + \left(\frac{Q}{b}\right)^n = 1 \ ,$$

where a and b are two constants. The shape of the envelope is linked to the micromechanics of compaction. Our data may be fitted to the theoretical relation using a value of n in the range of 1–1.2.

5.2. Interplay of Compaction and Dilatancy During the Formation of Compaction Bands

[40] Seismic velocities increase during hydrostatic pressure build up and during initial axial loading (Figure 4), likely due to the progressive closure of preexisting microcracks. Previous studies of *Fortin et al.* [2005], *Ayling et al.* [1994], *Read et al.* [1994], and *Scott et al.* [1993] demonstrated that elastic wave velocities are affected by two competing mechanisms during the compaction of porous sandstone: cracking and porosity decrease. Our experimental results show that cracking is the dominant effect, so that the formation of compaction bands was accompanied by a large decrease in elastic wave velocities (Figure 4). Our data here also show that the formation of compaction bands is associated with a small anisotropy of elastic properties. The two values of C_{11} and C_{33} differ by about 6% at a porosity reduction of about 3% (Figure 5 and see section 3.2). This implies that intragranular and intergranular cracking are for the most part randomly oriented in the compaction band.

[41] The SEM micrographs (Figures 11 and 12) also convincingly demonstrate that the dominant micromechanism leading to the formation of compaction bands is grain crushing. This is in agreement with observations on the compaction of Berea sandstone [*Ménendez et al.*, 1996] and Castelgate sandstone [*DiGiovanni et al.*, 2000], but also with observations of compaction bands in Bentheim sandstone [*Baud et al.*, 2004]. *Mair et al.* [2000] and *El Bied et al.* [2002] report similar experimental observations of compacting shear bands in highly porous rocks. Moreover, our SEM micrographs also show that within a compaction band,

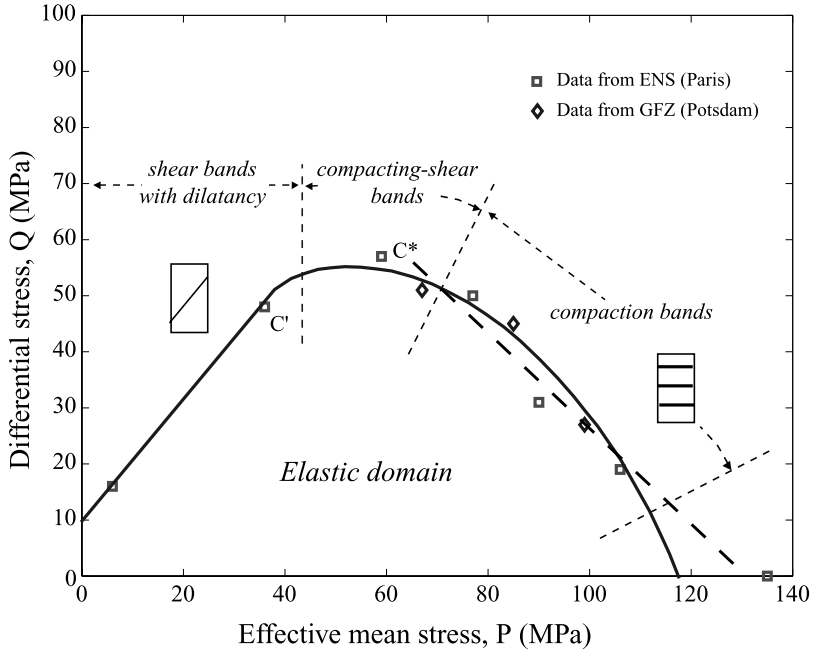

Figure 13. Yield envelopes for brittle strength and shear-enhanced compaction. Stress state C^* at the onset of shear enhanced compaction (effective confining pressure higher than 30 MPa) and stress state C' at the onset of shear-induced dilatation for brittle fracture are shown in stress space. Note that the compactive yield envelope approximately follows a straight line with a negative slope.

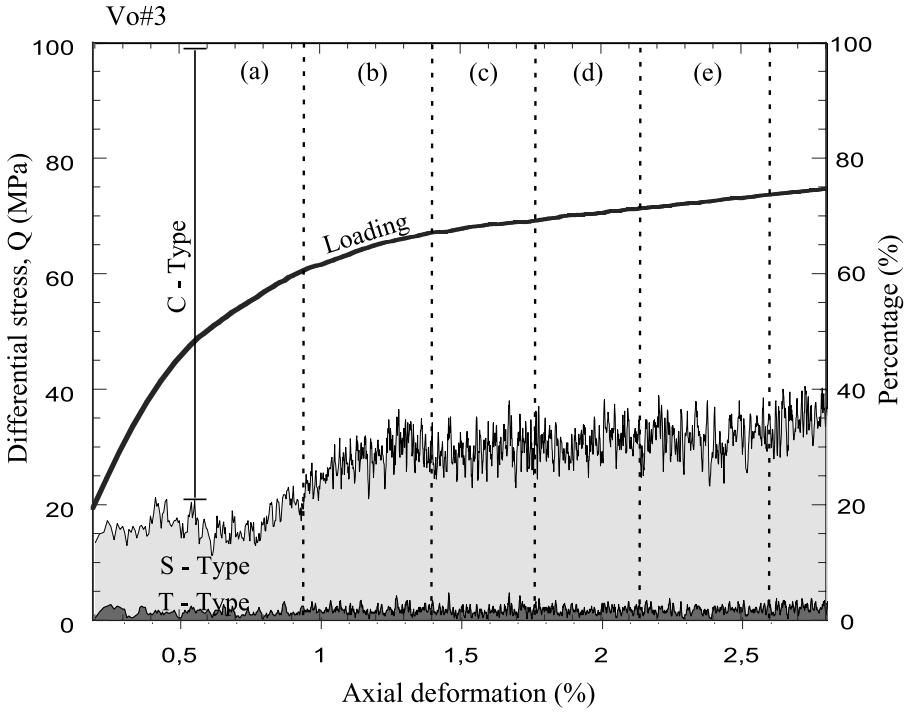

Figure 14. Modes of crack propagation during the formation of compaction bands. The solid black curve is the differential stress versus axial strain from triaxial compression test Vo3 at 80 MPa confining pressure. The different strain increments are defined in Figures 6a and 7. Color code indicates AE-source-type distribution during loading, with C type in white, S type in gray, and T type in black. Relative percentages of each event type at a given strain increment can be determined from the relative percentages of white, gray, and black regions from the right vertical axis. C-, S-, and T-type events possibly represent signals radiated from pore collapse, shear, and tensile cracks respectively. C-type events, indicating pore collapse, represent the dominant source type recorded before and during the formation of compaction bands (~70% of the source mechanisms).

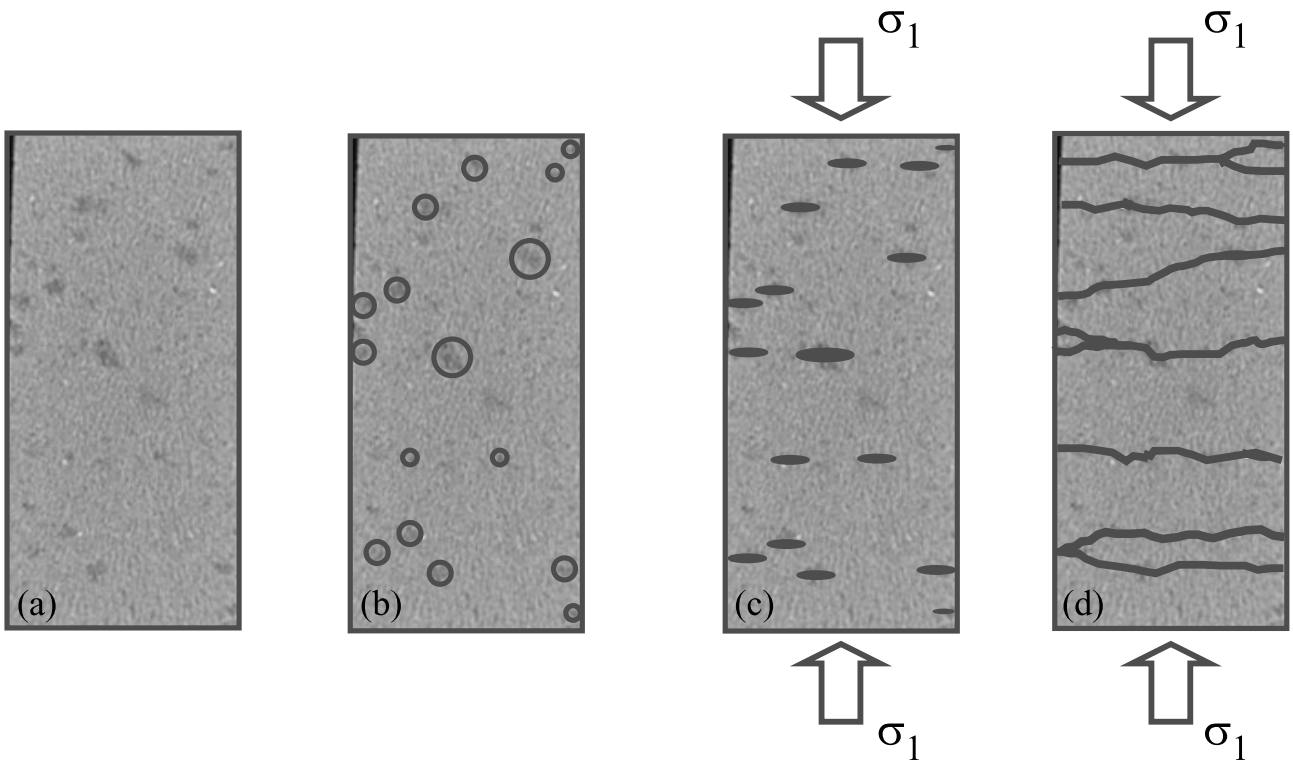

Figure 15. (a) Section across intact specimen (from a medical X-ray scanner) of Bleurswiller sandstone. The darker patches indicate zones of high porosity, (b–d) Conceptual model. Compaction bands may nucleate at high-porosity patches (circled in Figure 15b) and grow laterally across the sample, as shown in Figures 15c and 15d.

the orientations of cracks are highly variable, which is in agreement with the fact that the elastic anisotropy remains small.

5.3. Physics Behind the Three Phases of Microcracking

[42] AE focal mechanisms allows for the determination of the modes of crack propagation [*Lei et al.*, 1992; *Zang et al.*, 1998]. In our experiments, local AE source mechanisms were separated into tensile-type (T), shear-type (S), and implosion-type (C) events using the distribution of *P* wave first motions representing tensile cracks, shear cracks, and pore collapse, respectively [*Stanchits et al.*, 2001]. In experiments performed at a confining pressure of 80 MPa, we found that implosion-type events represent the dominant source type recorded before and during the formation of compaction bands (Figure 14). We relate C-type events to pore collapse. S- and C-type events represent about 26% and 70% of the source mechanisms, respectively, and tensile cracks represent less than 4%. The observations are in agreement with the studies of *Zang et al.* [2000] and *Lei et al.* [1992, 2000] who found that shear failure of sandstone was dominated by shear cracking and pore collapse.

[43] The observations of postdeformation microstructures predominantly show complex pore collapse structures. Individual shear cracks are typically not observed and shear displacements associated with pore collapse may be too small to be discriminated.

5.4. Role of Heterogeneity

[44] The effect of rock heterogeneities on processes leading to shear localization in rock has been investigated repeatedly. For example, *Holcomb and Costin* [1986] have performed tests on banded sandstones. The authors observed the formation of AE clusters during early loading stages indicating nonuniform microcracking due to local variations in material properties. *Papka and Kyriakides* [1998] studied the effect of heterogeneity on localized compaction in honeycombs during uniaxial and biaxial testing. They found that collapse of the pore space may have initiated from small geometric imperfections. *Blazy* [2003] studied the compressive and tensile deformation of aluminium foams. He found that compaction localization initiates in regions of a sample where the porosity is higher than the average porosity of the foam.

[45] More recently, *Katsman et al.* [2005] modeled the formation of compaction bands in high-porosity rock represented by a hexagonal lattice of springs. They introduced a disorder parameter D which accounted for the textural heterogeneity of the rock. They analyzed the effect of variations in D on the formation of compaction bands between $D = 0$ (no disorder) and $D = 0.17$ (strongly disordered). In a homogeneous material ($D = 0$) discrete compaction bands nucleate at the specimen boundaries in agreement with postmortem observations on Bentheim sandstone [*Klein et al.*, 2000] and Diemelstadt sandstone [*Baud et al.*, 2004]. For disordered heterogeneous materials, the model shifts the nucleation sites into the interior of the specimen. The shape of the compaction bands found by *Katsman et al.* [2005] in their simulations (shown in their Figures 10 and 11) may be compared to the shape of the AE hypocenter clusters from our experiments (Figures 7 and 8).

[46] The porosity distribution of an intact specimen of Bleurswiller sandstone is revealed in tomographic images produced in a medical X-ray scanner (Figure 15). This technique provides a spatial view of the local density distribution inside the specimen where high porosity regions appear as dark patches inside the specimen. We suggest that the observed compaction bands may nucleate by local pore collapse in these high-porosity regions. The incipient bands then grow laterally and coalesce with other high-porosity zones ultimately crosscutting the entire sample.

[47] As a consequence, the variation in the geometry and microstructures of the compaction bands may be a function of the rock heterogeneity and textural instabilities. *Olsson and Holcomb* [2000] recorded AE locations during localized compaction in Castlegate sandstone. They did not observe discrete compaction bands, but rather observed compaction nucleating at the top and bottom ends of the specimens. With progressive strain a compaction front propagated parallel to the compression direction into the sample interior. It is possible that this different behavior arises because porosity in Castlegate sandstone may be more homogeneous than in Bleurswiller sandstone samples.

5.5. Comparison of Laboratory and Field Observations of Compaction Bands

[48] *Klein et al.* [2001] conducted experiments on Bentheim sandstone, a well-cemented rock containing ~99% quartz with an initial porosity of ~25%. They observed compaction bands when the samples were subjected to high confining pressures in the range 180–400 MPa. In our experiments, Bleurswiller sandstone contains 50% quartz, 30% feldspars, and 20% oxides micas and the initial porosity is ~25%. Our observations show that compaction bands occur at lower pressures (i.e., 60–100 MPa). Yet this latter range of pressures is not that of field conditions. However, these observations suggest that in addition to variations in porosity other material properties such as mineral composition and cement type may influence compaction band formation.

[49] Compaction bands observed macroscopically in the field [e.g., *Mollema and Antonellini*, 1996] appear to be very similar to those produced in experiments. However, microstructure studies of field specimens reveal significantly less grain crushing than is found in samples deformed experimentally. This striking difference in microstructures indicates that compaction bands may be produced by different deformation mechanisms which may operate at lower stresses and lower strain rates in the field. In particular, it remains unclear to what extend compaction is produced by frictional sliding of intact grains facilitated by stress corrosion and/or solution-precipitation mechanisms.

[50] Compaction bands result in a localized reduction of porosity which can be directly related to changes in pore topology. As a consequence, (1) the radii of pores in a compaction band are lower than in the nondeformed rock, and (2) the specific surface area in a compaction band is higher than in the nondeformed rock. These two mechanisms facilitate the precipitation of minerals [e.g., *Rutter*, 1976; *Tenthorey et al.*, 1998; *Yasuhara et al.*, 2003] and could heal the grain crushing-induced cracks. Solution-precipitation mechanisms might transform compaction bands like those observed in our experiments into cemented compaction bands similar to those observed in the field.

[51] Moreover, in field conditions, the strain rate is much lower than it is in laboratory conditions. We observed in our experiments that intergranular and intragranular cracking is pervasive in compaction bands [see also *Klein et al.*, 2001; *Baud et al.*, 2004]. In field conditions, we suggest that the cracking process could be subcritical crack growth (when water has access to crack tips) instead of the comparatively rapid crack growth which occurs in our experiments. Subcritical crack growth is slow and depends on microstructural features such as grain size, porosity, mineralogy, and the shape of the grain boundaries [e.g., *Atkison*, 1984]. Intergranular subcritical crack growth could preferentially appear at low strain rates in field conditions. Porosity reduction could possibly take place in such cases without grain crushing.

[52] Healing and subcritical crack growth are just two possible processes which could explain the differences between field and laboratory microstructures. Both depend on the presence of fluids. More experiments are necessary to investigate the influence of strain rate and chemically reactive fluids on the micromechanics of compaction.

6. Conclusions

[53] We investigated the formation of localized compaction bands in Bleurswiller sandstone at confining pressures of 60–100 MPa by combining advanced acoustic emission techniques, elastic wave velocity measurements, and microstructural studies.

[54] AE hypocenter distribution closely mirrors the location of compaction bands as observed in deformed samples.

[55] Nucleation and growth of compaction bands occurs by localized grain crushing and pore collapse. Nucleation is strongly affected by experimental stress boundary conditions (i.e., end cap friction) and material heterogeneities (i.e., high local porosity).

[56] Initial loading and associated crack closure produced a transient velocity increase. However, with progressive loading and localized shear-enhanced compaction of the samples P and S wave velocities decreased drastically. The velocity decrease is assumed to reflect the enhanced microcracking associated with grain crushing and pore collapse.

[57] The existence of compaction bands has important implications on the field scale. Compaction and compacting shear bands have been recognized as potential barriers for subsurface fluid flow [*Mollema and Antonellini*, 1996; *Antonellini et al.*, 1999]. Compaction bands are characterized by grain translation, pore collapse, and grain crushing that result in porosity and permeability reduction. The systematic organization of compaction bands within poorly consolidated sand and sandstone may result in a complex permeability structure that effectively localizes and compartmentalizes flow and subsurface fluids.

[58] **Acknowledgments.** This work benefited from discussions with many scientists. Among them, the authors would like to particularly thank Alexandre Schubnel, Eric Grueschow, and John Rudnicki. We are also grateful to Stephan Gehrmann (GeoForschungsZentrum, Potsdam) for aid in preparing the thin sections. The first author was supported by the Deutscher Akademischer Austausch Dienst (DAAD). We also thank the

two reviewers and the Associate Editor for their insightful reviews. Partial financial support for this work was provided by the CNRS.

References

Ayling, M. R., P. G. Meredith, and S. Murrell (1994), Microcracking during triaxial deformation of porous rocks monitored by changes in rock physicical properties, I. Elastic-wave propagation measurements on dry rocks, *Tectonophysics*, *245*, 205–221.

Atkison, B. K. (1984), Subcritical crack-growth in geological-materials, *J. Geophys. Res.*, *89*, 4077–4114.

Antonellini, M., A. Aydin, and L. Orr (1999), Outcrop-aided characterization of a faulted hydrocarbon reservoir: Arroyo Grande oil field, California, USA, in *Faults and Subsurface Fluid Flow in the Shallow Crust*, edited by W. C. Haneberg et al., pp. 7–26, AGU, Washington D. C.

Baud, P., E. Klein, and T.-F. Wong (2004), Compaction localization in porous sandstones: Spatial evolution of damage and acoustic emission activity, *J. Struct. Geol.*, *26*, 603–624.

Bésuelle, P. (2001), Compacting and dilating shear bands in porous rock, *J. Geophys. Res.*, *106*, 13,435–13,442.

Bésuelle, P., and J. W. Rudnicki (2004), Localization: Shear bands and compaction bands, in *Mechanics of Fluid-Saturated Rocks*, *Int. Geophys. Ser.*, vol. 89, edited by Y. Guéguen and M. Boutéca, pp. 219–323, Elsevier, New York.

Blazy, J. S. (2003), Comportement mécanique des mousses d'aluminium: Caractérisations expérimentales sous sollicitations complexes et simulations numériques dans le cadre de l'élasto-plasticité compressible, Thèse de doctorat, Ecole des Mines de Paris, Paris.

DiGiovanni, A., J. T. Fredrich, D. J. Holcomb, and W. A. Olsson (2000), Micromechanics of compaction in an analogue reservoir sandstone, *Proceedings of the North American Rock Mechanics Symposium, July 31, 2000*, edited by J. Girard et al., pp. 1153–1158, A. A. Balkema, Brookfield, Vt.

El Bied, A., J. Sulem, and F. Martineau (2002), Microstructure of shear zone in Fontainebleau sandstone, *Int. J. Rock. Mech. Min. Sci Geomech. Abstr.*, *39*, 917–932.

Fortin, J., P. Baud, and T.-F. Wong (2003), Mechanical compaction of Diemelstadt: From compacting shear bands to pure compaction bands, paper presented at EGS-AGU-EUG Joint Assembly, Nice, France.

Fortin, J., A. Schubnel, and Y. Guéguen (2005), Elastic wave velocities and permeability evolution during compaction of Bleurswiller sandstone, *Int. J. Rock. Mech. Min. Sci Geomech.*, *42*, 873–889.

Grueschow, E. (2005), Yield cap constitutive models for predicting compaction localization in high porosity sandstone, dissertation, Northwestern Univ., Evanston, Ill.

Haimson, B. C. (2001), Fracture-like borehole breakouts in high porosity sandstone: Are they caused by compaction bands?, *Phys. Chem. Earth, Part A*, *26*, 15–20.

Holcomb, D. J., and L. S. Costin (1986), Detecting damage surfaces in brittle materials using acoustic emissions, *J. Appl. Mech.*, *108*, 536–544.

Holcomb, D. J., and W. A. Olsson (2003), Compaction localization and fluid flow, *J. Geophys. Res.*, *108*(B6), 2290, doi:10.1029/2001JB000813.

Issen, K. A., and J. W. Rudnicki (2000), Conditions for compaction bands in porous rock, *J. Geophys. Res.*, *105*, 21,529–21,536.

Katsman, R., E. Aharonov, and H. Scher (2005), Numerical simulation of compaction bands in high-porosity sedimentary rock, *Mech. Mater.*, *37*, 143–162.

Klein, E., P. Baud, T. Reuschle, and T.-F. Wong (2001), Mechanical behaviour and failure mode of Bentheim sandstone under triaxial compression, *Phys. Chem. Earth, Part A*, *26*, 21–25.

Lei, X., O. Nishizawa, K. Kusunose, and T. Satoh (1992), Fractal structure of the hypocenter distributions and focal mechanism solutions of acoustic emission in two granites of different grain sizes, *J. Phys. Earth.*, *40*, 617–634.

Lei, X., K. Kusunose, M. V. M. S. Rao, O. Nishizawa, and T. Satoh (2000), Quasi-static fault growth and cracking in homogeneous brittle rock under triaxial compression using acoustic emission monitoring, *J. Geophys. Res.*, *105*, 6127–6139.

Lockner, D. A. (1993), The role of acoustic emission in the study of rock fracture, *Int. J. Rock Mech. Min. Sci. Geomech.*, *30*, 883–899.

Mair, K., I. Main, and S. Elphick (2000), Sequential growth of deformation bands in the laboratory, *J. Struct. Geol.*, *22*, 25–42.

Mavko, G., T. Mukerji, and J. Dvorkin (1998), *The Rock Physics Handbook*, Cambridge Univ. Press, New York.

Ménendez, B., W. Zhu, and T.-F. Wong (1996), Micromechanics of brittle faulting and cataclastic flow in Berea sandstone, *J. Struct. Geol.*, *18*, 1–16.

Mollema, P. N., and M. A. Antonellini (1996), Compaction bands: A structural analog for anti-mode I crack in aeloian sandstone, *Tectonophysics*, *267*, 209–228.

Nelder, J. A., and R. Mead (1965), A simplex method for function minimization, *Comput. J.*, *7*, 308–313.

Olsson, W. A. (1999), Theoretical and experimental investigation of compaction bands in porous rock, *J. Geophys. Res.*, *104*, 7219–7228.

Olsson, W. A., and D. J. Holcomb (2000), Compaction localization in porous rock, *Geophys. Res. Lett.*, *27*, 3537–3540.

Papka, S. D., and S. Kyriakides (1998), Biaxial crushing of honeycombs - Part I: Experiments, *Int. J. Solids. Struct.*, *36*, 4367–4396.

Paterson, M. S. (1978), *Experimental Rock Deformation: The Brittle Field*, Springer, New York.

Read, M. D., M. R. Ayling, P. G. Meredith, and S. Murrell (1994), Microcracking during triaxial deformation of porours rocks monitored by changes in rock physical properties, II. Pore volumometry and acoustic emission measurements on water-saturated rocks, *Tectonophysics*, *245*, 223–235.

Rudnicki, J. W. (2004), Shear and compaction band formation on an elliptic yield cap, *J. Geophys. Res.*, *109*, B03402, doi:10.1029/2003JB002633.

Rudnicki, J. W., and J. R. Rice (1975), Conditions for the localization of deformation in pressure-sensitive dilatant materials, *J. Mech. Phys. Solids*, *23*, 371–394.

Rutter, E. H. (1976), The kinetics of rock deformation by pressure solution, *Philos. Trans. R. Soc. London, Ser. A*, *238*, 725–740.

Schubnel, A., J. Fortin, L. Burlini, and Y. Guéguen (2005), Damage and elastic recovery of calcite-rich rocks deformed in the cataclastic regime, *Geol. Soc. London*, *245*, 203–221.

Scott, T. E., Q. Ma, and T. C. Roegiers (1993), Acoustic velocity changes during shear enhanced compaction of sandstone, *Int. J. Rock Mech. Min. Sci. Geomech.*, *30*, 763–769.

Stanchits, S., A. Zang, and G. Dresen (2001), Focal mechanisms of acoustic emission events during fault propagation and friction sliding, *Eos Trans. AGU*, *82*(47), Fall Meet. Suppl., Abstract T51A-0847.

Tenthorey, E., C. H. Scholz, and E. Aharonov (1998), Precipitation sealing and diagenesis, *J. Geophys. Res.*, *103*, 23,951–23,967.

Thomsen, L. (1986), Weak elastic anisotropy, *Geophysics*, *51*, 1954–1966.

Underwood, E. E. (1970), *Quantitative Stereology*, Addison-Wesley, Boston, Mass.

Vajdova, V., P. Baud, and T.-F. Wong (2004), Permeability evolution during localized deformation in Bentheim sandstone, *J. Geophys. Res.*, *109*, B10406, doi:10.1029/2003JB002942.

Walsh, J. B. (1965), The effect of cracks on the compressibility of rock, *J. Geophys. Res.*, *70*, 381–389.

Wong, T.-F., C. David, and W. Zhu (1997), The transition from brittle faulting to cataclastic flow in porous sandstone: Mechanical deformation, *J. Geophys. Res.*, *102*, 3009–3025.

Yasuhara, H., D. Elsworth, and A. Polak (2003), A mechanistic model for compaction of granular aggregates moderated by pressure solution, *J. Geophys. Res.*, *108*(B11), 2530, doi:10.1029/2003JB002536.

Zang, A., F. C. Wagner, S. Stanchits, G. Dresen, R. Andresen, and M. A. Haidekker (1998), Source analysis of acoustic emissions in Aue granite cores under symmetric and asymmetric compressive loads, *Geophys. J. Int.*, *135*, 1113–1130.

Zang, A., F. C. Wagner, S. Stanchits, C. Janssen, and G. Dresen (2000), Fracture process zone in granite, *J. Geophys. Res.*, *105*, 23,651–23,661.

Zhang, J., T.-F. Wong, and D. M. Davis (1990), Micromechanics of pressure-induced grain crushing in porous rocks, *J. Geophys. Res.*, *95*, 341–352.

G. Dresen and S. Stanchits, GeoForschungsZentrum, Telegrafenberg D423, Potsdam, D-14473 Germany.

J. Fortin and Y. Guéguen, Laboratoire de Géologie, Ecole Normale Supérieure, 24 rue Lhomond, F-75005, Paris, France. (fortin@geologie.ens.fr)